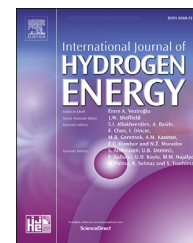


Available online at [www.sciencedirect.com](http://www.sciencedirect.com)

ScienceDirect

journal homepage: [www.elsevier.com/locate/ijhydene](http://www.elsevier.com/locate/ijhydene)

# Theoretical study of M–H (M=Ti, V, Zr or Nb) structure phase diagram at high pressures

Xue-Yu Zhao <sup>a</sup>, Xiao-Bao Yang <sup>a,b</sup>, Liuzhang Ouyang <sup>b,c</sup>, Yu-Jun Zhao <sup>a,b,\*</sup>

<sup>a</sup> Department of Physics, South China University of Technology, Guangzhou, Guangdong 510640, China

<sup>b</sup> Key Laboratory of Advanced Energy Storage Materials of Guangdong Province, South China University of Technology, Guangzhou, Guangdong 510640, China

<sup>c</sup> School of Materials Science and Engineering, South China University of Technology, Guangzhou, Guangdong 510640, China

## ARTICLE INFO

### Article history:

Received 2 December 2018

Received in revised form

21 March 2019

Accepted 27 March 2019

Available online 17 April 2019

### Keywords:

Structure prediction

First-principles calculation

Metal hydride

Phase transition

Hydrogen storage

## ABSTRACT

We have performed structure searches for titanium (Ti) hydrides, vanadium (V) hydrides, zirconium (Zr) hydrides and niobium (Nb) hydrides under ambient and high pressure up to high hydrogen content using CALYPSO method combined with first-principles calculations. Ten novel stable phases,  $R\bar{3}$ -TiH<sub>3</sub>,  $P4_2/mnm$ -TiH<sub>3</sub>,  $Ibam$ -TiH<sub>2.5</sub>,  $Cccm$ -VH,  $Pna2_1$ -ZrH<sub>4</sub>,  $R\bar{3}$ -ZrH<sub>3</sub>,  $Pm\bar{3}n_1$ -ZrH<sub>3</sub>,  $R\bar{3}m$ -ZrH<sub>2.5</sub>,  $P2/c$ -NbH<sub>2.5</sub> and  $P4_2/mcm$ -NbH<sub>2.5</sub> were discovered under various pressures. In particular, the high hydrogen content  $Pna2_1$ -ZrH<sub>4</sub> can be stabilized at 4–12 GPa. The detailed crystal structure, dynamical stability and electronic structure are also investigated for those novel stable phases. Combined with earlier predicted structures, comprehensive pressure–chemical potential ( $P$ - $\Delta\mu_H$ ) phase diagrams are constructed for these M–H systems.

© 2019 Hydrogen Energy Publications LLC. Published by Elsevier Ltd. All rights reserved.

## Introduction

Metal hydrides with large hydrogen storage capacity and high safety have been receiving widespread attention and extensive study as promising hydrogen storage materials [1,2]. Moreover, strong electron-phonon coupling in high hydrogen content hydrides indicates the hydrides as great candidates of high-temperature superconductors, which also receiving intensive attention [3,4].

Ti, V, Zr and Nb are used as components of hydrogen storage alloys frequently, especially the vanadium based hydrogen storage materials [5–7], which have high hydrogen

storage capacity (4 wt%) and high hydrogen diffusivity. Nb with high hydrogen permeability [8,9] is often used in the alloying of metal hydride systems to alter the hydrogenation properties. For example, partial Nb substitution can improve the cycle durability of Ti–Cr–V alloys with no effect to the hydrogen storage capacity [10,11]. The Ti-based AB-type alloys [12,13], the Ti-based AB<sub>2</sub>-type alloys [14–16] and the Zr-based AB<sub>2</sub>-type alloys [17,18] are also strong candidates for hydrogen storage. TiFe alloys [12,13], the typical Ti-based AB-type alloys, attracted extensive attention due to their good reversibility, low operation temperature and relatively low price. Ti-based AB<sub>2</sub>-type alloys, such as TiMn<sub>2</sub> [15,16], have been extensively investigated due to their easy activation, good hydrogenation/

\* Corresponding author. Department of Physics, South China University of Technology, Guangzhou, Guangdong 510640, China.

E-mail address: [zhaoyj@scut.edu.cn](mailto:zhaoyj@scut.edu.cn) (Y.-J. Zhao).

<https://doi.org/10.1016/j.ijhydene.2019.03.210>

0360-3199/© 2019 Hydrogen Energy Publications LLC. Published by Elsevier Ltd. All rights reserved.

dehydrogenation kinetics and relatively low cost. ZrV<sub>2</sub> alloys [17,18], one of the typical Zr-based AB<sub>2</sub>-type alloys, are known for easy activation and low equilibrium pressure. As the transition metals, Ti, V, Zr and Nb can also serve as additives to improve hydrogen absorption/desorption kinetics in other metal hydride systems [19,20].

Increasing the valence of metal ions can effectively enhance the hydrogen storage capacity. Although there are high oxidation states of +4 or +5 for various inorganic compounds of Ti, V, Zr and Nb. Unfortunately, only dihydrogen compounds of M–H system (M = Ti, V, Zr or Nb) have been obtained in experiments [21–24]. It is curious if the preparation conditions of high hydrogen content hydrides are feasible.

Pressure is an important factor for preparation and synthesis of materials [25–28]. For the metal hydrides, it not only helps to get new phase but also conduces to the stability of high hydrogen content hydrides since higher hydrogen chemical potential can be obtained at high pressures. The structures and phase transitions of dihydrogen and lower valence compounds is well studied [29–37], including the phase transition in dihydrogen compounds of the Ti, V, Zr and Nb under high pressure [38–40]. In contrast, the structures of hydrides with higher hydrogen content are not well understood.

CALYPSO method is a structure prediction method based on particle swarm optimization algorithm, which has successfully searched various elements [41,42], binary [43,44] and ternary [45–47] compounds. Recently, structural searches for hydrides of Ti, V, Zr and Nb focusing on superconductivity are performed [48–54]. High hydrogen content hydrides, such as phases of TiH<sub>6</sub> [48], VH<sub>8</sub> [52], ZrH<sub>6</sub> [51], and NbH<sub>6</sub> [54], were uncovered at high pressure. However, the same phases, for example, the *Fm* $\bar{3}$ *m*-VH<sub>3</sub>, have different stability ranges in their respective reports. The stable phases at a certain pressure are also disputable between their discoveries, which deserve further discussion.

In this work, we performed a structure search on MH<sub>x</sub> (M = Ti, V, Zr and Nb; x ≤ 4) in the pressure range of 0–100 GPa at zero temperature, using the CALYPSO method, combining with first-principles calculation. Ten novel stable phases, including high hydrogen content hydrides, TiH<sub>3</sub>, ZrH<sub>4</sub>, and NbH<sub>2.5</sub>, were discovered under various pressures. The pressure and chemical potential range in phase diagrams for the stable phases were calculated. The dynamical stability and electronic structures were also been investigated. Our results will provide guidance for the preparation of high hydrogen content hydrides in experiments.

## Computational details

The structures of MH<sub>x</sub> (M = Ti, V, Zr or Nb; x ≤ 4) were predicted by using the CALYPSO code [55,56]. Crystal structures were searched with simulation cells containing up to 8 formula units at pressures of 0 and 70 GPa. Each prediction was carried out for 30 to 45 generations. The total number of structures per generation, i.e., the population size, was set to

30. Local PSO algorithm was adopted in searches. The structures of first generation were produced randomly, while 60% of the structures was produced by PSO in the following generations, with the others generated randomly. About 3000 structures were calculated for each stoichiometry.

The simulated crystal structures were visualized as implemented in the VESTA program [57]. The underlying *ab initio* structural relaxations and electronic structure calculations were based on density functional theory (DFT) method with the Perdew-Burke-Ernzerhof (PBE) [58] exchange-correlation functional, as implemented in the Vienna Ab-initio Simulation Package (VASP) [59]. The projector augmented wave (PAW) [60] method was employed, with the 4s<sup>1</sup>3d<sup>3</sup>, 3p<sup>6</sup>4s<sup>1</sup>3d<sup>4</sup>, 4s<sup>2</sup>4p<sup>6</sup>5s<sup>2</sup>4d<sup>2</sup>, 4p<sup>6</sup>5s<sup>1</sup>4d<sup>4</sup> and 1s<sup>1</sup> as valence electrons for Ti, V, Zr, Nb and H, respectively. The energy cutoff of 600 eV for the plane-wave expansion and the Brillouin zone integration grid spacing of 2π × 0.032 Å<sup>-1</sup> was used to ensure that all the enthalpy calculations were converged to less than 1 meV per atom. The phonon calculations were carried out using a supercell approach as implemented in the phonopy code [61]. The enthalpy of formation per formula unit for M<sub>x</sub>H<sub>y</sub>, ΔH<sub>f</sub>, was calculated as:

$$\Delta H_f = (H_{M_xH_y} - xH_M - y\mu_H)/x, \quad (1)$$

where H<sub>M<sub>x</sub>H<sub>y</sub></sub> and H<sub>M</sub> are the calculated enthalpy of M<sub>x</sub>H<sub>y</sub> and M and respectively, μ<sub>H</sub> is the chemical potential of hydrogen. Δμ<sub>H</sub> is chemical potential of hydrogen with respect to H<sub>2</sub> molecule at 0 GPa.

$$\Delta\mu_H = \mu_H - H_{H_2}/2, \quad (2)$$

where H<sub>H<sub>2</sub></sub> is the calculated enthalpy of H<sub>2</sub> molecule.

## Results and discussion

### Ti-H system under ambient pressure

The structures of TiH<sub>x</sub> (x = 2, 2.5, 3, 4) were predicted at ambient pressure. Detailed structural parameters of Ti-H compounds are listed in Table S1. For TiH<sub>2</sub>, we find the tetragonal *I4/mmm* phase (Fig. 1a) as the most stable structure, which is in good agreement with previous results [40]. In this structure, each conventional cell contains two formula units. Ti atoms located at the 2*b* Wyckoff positions form a body-centered tetragonal (bct) sublattice. H atoms situated in the tetrahedral sites, occupy the 4*d* positions of *I4/mmm*. The most stable structure of TiH<sub>2.5</sub> at ambient pressure is the trigonal *R* $\bar{3}$ *m* phase (Fig. 1c). In this structure, each conventional cell contains four Ti atoms and ten H atoms. There are half of the Ti atoms, each surrounded by eight H atoms, while each of the others is surrounded by eleven H atoms. These two kinds of Ti-centered polyhedrons are arranged in the *c* direction alternately. Four-fifths of H atoms are located at the tetrahedral voids, while each of the others is surrounded by three Ti atoms. The TiH<sub>3</sub> we predicted under ambient pressure is a structure with *P6*<sub>3</sub>/*m* symmetry (Fig. 1e), which contains two TiH<sub>3</sub> formula units in each conventional cell. The Ti and H atoms are located at the 2*d* and 6*h* Wyckoff positions

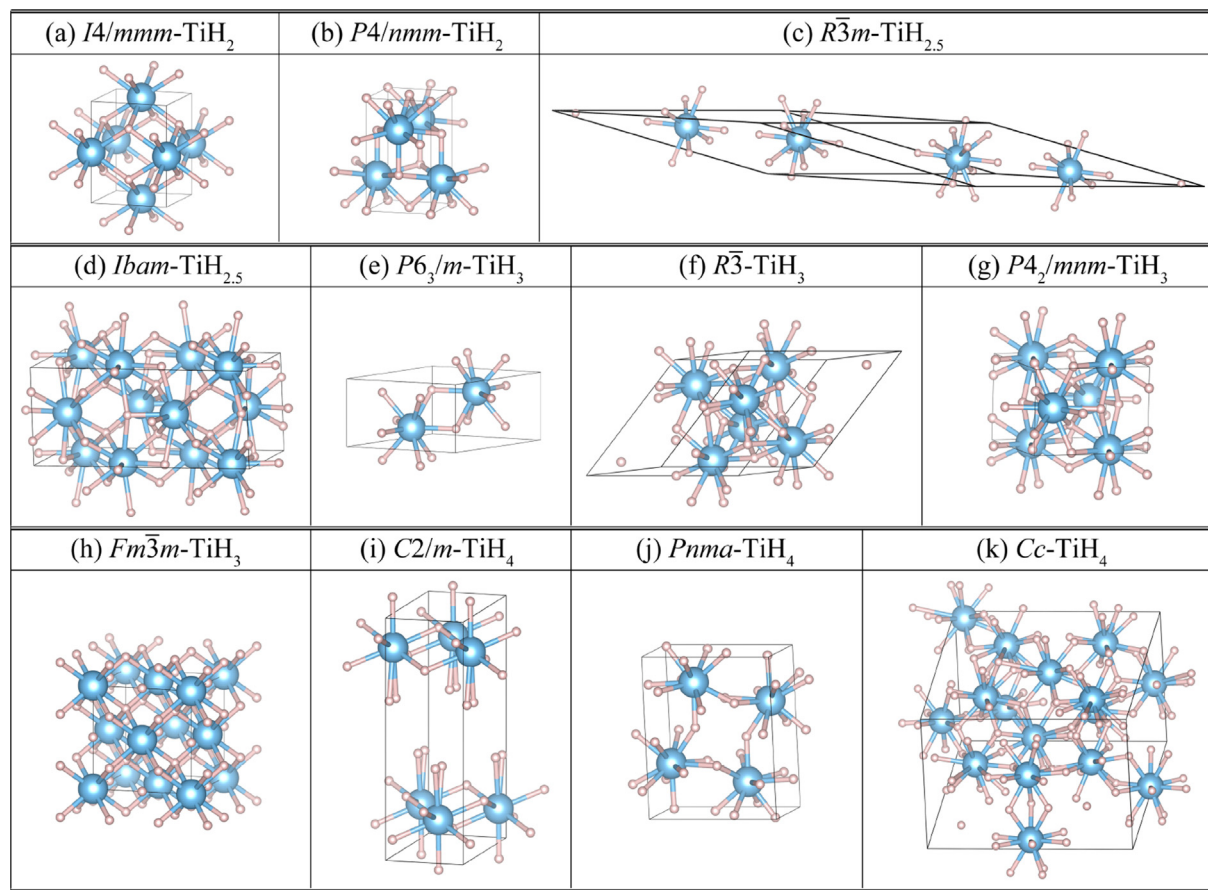


**Fig. 1** – Optimized crystal structures of Ti-H systems. (a)  $I4/mmm$ -TiH<sub>2</sub>, (b)  $P4/nmm$ -TiH<sub>2</sub>, (c)  $R\bar{3}m$ -TiH<sub>2.5</sub>, (d)  $Ibam$ -TiH<sub>2.5</sub>, (e)  $P6_3/m$ -TiH<sub>3</sub>, (f)  $R\bar{3}$ -TiH<sub>3</sub>, (g)  $P4_2/mnm$ -TiH<sub>3</sub>, (h)  $Fm\bar{3}m$ -TiH<sub>3</sub>, (i)  $C2/m$ -TiH<sub>4</sub>, (j)  $Pnma$ -TiH<sub>4</sub>, and (k)  $Cc$ -TiH<sub>4</sub>. Blue and small pink balls denote Ti and H atoms respectively. (For interpretation of the references to colour in this figure legend, the reader is referred to the Web version of this article.)

respectively. Each Ti atom is surrounded by nine H atoms, while every H atom has three neighbor Ti atoms. For TiH<sub>4</sub>, the most stable phase monoclinic  $C2/m$  (Fig. 1i) shows a layered structure, composed of the Ti-centered polyhedrons. The Ti atom is surrounded by nine H atoms, which makes up a cube with a vertex replaced by a pair of H atoms that are 0.794 Å apart. The pairs of H atoms are located at the surface of the layers and have the same orientation. The Ti-centered polyhedrons within layers are connected by common edges.

The stability among different stoichiometry for titanium hydrides was evaluated by formation enthalpy with respect to the  $\omega$  phase of Ti [62] and the H<sub>2</sub> molecule. The metastable structures of  $P4_2/mnm$  for TiH [22,63] also appears as a reference in the calculation. Fig. 2 shows the evolutions of formation enthalpy with chemical potential of H for titanium hydrides. The vertical dashed line passing through the zero divides the picture into two parts. The left side of the dashed line (the green area) represents the area where the chemical potential is in a reachable range, while the gray area to the right side requires unachievable conditions. The result indicates that only Ti and TiH<sub>2</sub> can be stable under ambient pressure. In order to find higher hydrogen content titanium hydrides, we may need predicting under higher pressure.

#### Ti-H system at high pressure

The structures of TiH<sub>x</sub> ( $x = 2, 2.5, 3, 4$ ) were searched up to 100 GPa. The predicted structures are displayed in Fig. 1 and the calculated enthalpies curves are shown in Fig. S2.

The  $I4/mmm$  phase (Fig. 1a), the most stable structure of TiH<sub>2</sub> at ambient pressure, becomes a metastable phase with the pressure increases beyond 75 GPa. Another tetragonal structure,  $P4/nmm$  phase (Fig. 1b), has the lowest enthalpy in TiH<sub>2</sub> when the pressure in the range of 75–100 GPa. In the  $P4/nmm$  structure, Ti atoms form a slightly distorted bct sublattice, with all the Ti atoms located at the 2c Wyckoff positions. Half of the H atoms are situated in the tetrahedral sites at the 2a positions. The others are situated in the octahedral sites at the 2c positions. Each conventional cell contains two formula units.

The  $Ibam$  phase (Fig. 1d) replaces the  $R\bar{3}m$  phase (Fig. 1c) as the most stable structure of TiH<sub>2.5</sub> when pressure up to 17 GPa. This structure contains eight TiH<sub>2.5</sub> formula units in each conventional cell. Ti atoms situated in 8j Wyckoff positions, form a face-centered tetragonal (fct) sublattice with distortion. Each Ti atom is surrounded by ten H atoms. H atoms surrounded by four Ti atoms can be divided into three

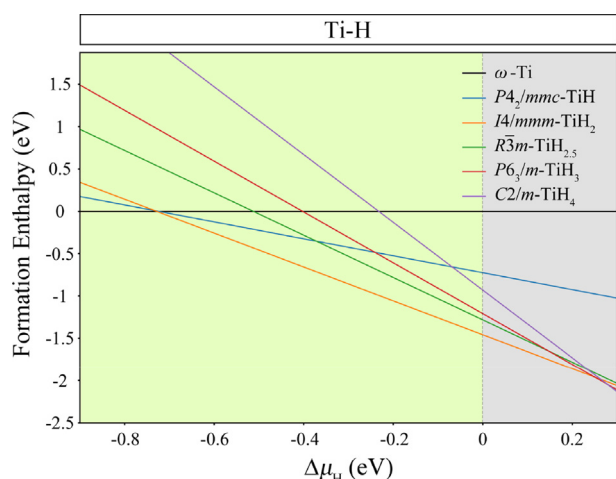


**Fig. 2 – Formation enthalpies of titanium hydrides as a function of hydrogen chemical potential at ambient pressure. Here, chemical potential of  $H_2$  is set to zero, beyond which the Ti-H compounds are unstable thermodynamically.**

categories according to the distortion degree of  $HTi_4$  tetrahedral, with H atoms located at the 4a, 8g, and 8j Wyckoff positions respectively.

$P6_3/m-TiH_3$  (Fig. 1e), the most stable phase between 0 and 4 GPa for  $TiH_3$ , whose fractional coordinates of H atoms move with the pressure, change its symmetry to  $P6_3/mmc$  (Fig. S1a) eventually when the pressure about 35 GPa. In this new metastable structure, the H atom is surrounded by four Ti atoms. When pressure is up to 4 GPa, a trigonal  $R\bar{3}$  phase (Fig. 1f) has the lowest enthalpy in  $TiH_3$ . This structure contains six  $TiH_3$  in a conventional cell. All of the Ti atoms are located at 6f Wyckoff positions, forming a hexagonal close-packed (hcp) sublattice. Two-thirds of H atoms located at 6f positions, are situated in the tetrahedral voids of the sublattice. The others are located at 2c positions, each surrounded by three Ti atoms. When pressure increases up to 68 GPa, a tetragonal  $P4_2/mnm$  phase (Fig. 1g) becomes more favorable. This structure can be regarded as a  $Pm\bar{3}n$  structure with minor distortion (can refer to the structure of  $Pm\bar{3}n$ - $ZrH_3$ , shown in Fig. 7f). In fact, the enthalpy of  $Pm\bar{3}n-TiH_3$  is almost the same as that of the  $P4_2/mnm-TiH_3$ . However, the  $Pm\bar{3}n-TiH_3$  is dynamically unstable in the corresponding pressure range (see Fig. S11a). In the structure of  $P4_2/mnm$  phase, each conventional cell contains four  $TiH_3$  formula units. Ti atoms form a distorted body-centered cubic (bcc) sublattice where H atoms occupy half of the tetrahedral voids. The coordination number of Ti atoms is twelve. Up to 77 GPa, a cubic phase with  $Fm\bar{3}m$  symmetry (Fig. 1h) predicted by Zhuang et al. [48], becomes the most stable of  $TiH_3$ . Structurally, each conventional cell contains four formula units. Ti atoms form a face-centered cubic (fcc) sublattice in which the H atoms occupy all the tetrahedral voids and octahedral voids. Each Ti atom surrounded by eight first nearest-neighbor H atoms and six second-nearest-neighbor H atoms.

For  $TiH_4$ , three structures in total, a  $Pnma$  phase (Fig. 1j), a  $Cc$  phase (Fig. 1k) and the mentioned  $C2/m$  phases (Fig. 1i) are predicted. The  $C2/m$  phases, the most stable structure of  $TiH_4$

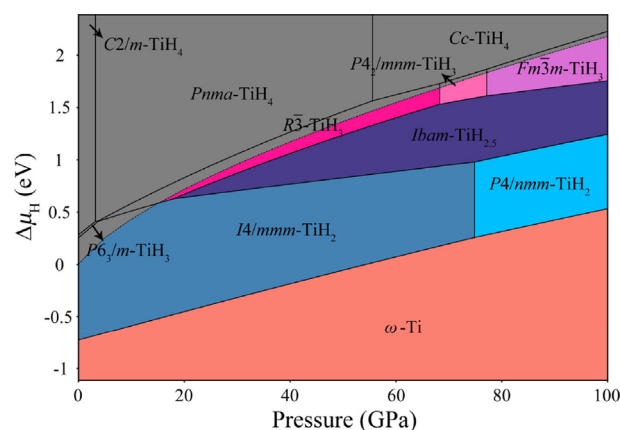


**Fig. 3 – Phase diagram of Ti-H system under pressure of 0–100 GPa. Structures in the gray region are unstable thermodynamically.**

at ambient pressure, loses the layered structure at the pressure about 55 GPa with the increasing coordination number of Ti. The orthorhombic  $Pnma$  phase becomes the most stable  $TiH_4$  between 3 and 56 GPa, composed by Ti-centered  $TiH_{11}$  polyhedrons. When the pressure is up to 56 GPa, the monoclinic  $Cc$  structure of  $TiH_4$ , containing four kinds of Ti-centered polyhedrons, becomes more favorable.

By calculating the range of stable phases at pressures between 0 and 100 GPa, we obtained the  $P-\Delta\mu_H$  phase diagram of Ti-H system (c.f. Fig. 3), to assess the stability among the predicted structures of Ti-H system under various pressures. The  $\omega$  phase for pure Ti [62] (Fig. S6a) and the hexagonal  $P6_3/m$  phase for H [64] were considered. Since the results of low hydrogen content hydrides have little impact on the search for high hydrogen content hydrides, high-pressure phases of those stoichiometric compositions were not considered. In the phase diagram, the chemical potential of  $P6_3/m-H$  is plotted as a dashed line, which increases along the pressure. The gray area above the dashed line denotes a region where the chemical potential of H atoms cannot reach. Different phases are separated by solid lines. The stable phases read from the phase diagram at ambient pressure correspond with Fig. 2, i.e., only Ti and  $TiH_2$  can be stable under ambient pressure. The result shows that  $TiH_3$  becomes stable under the pressure of 15 GPa with the  $R\bar{3}$  symmetry. Moreover, the  $P4_2/mnm-TiH_3$  and  $Fm\bar{3}m-TiH_3$  can be stable under 68–77 GPa and 77–100 GPa, respectively. Zhuang et al. [48] predicted a trigonal  $R32$  phase which transform into the  $Fm\bar{3}m-TiH_3$  at about 70 GPa. The reported  $R32-TiH_3$  has a similar structure to the  $R\bar{3}-TiH_3$  but is dynamically unstable in the corresponding pressure range (see Fig. S11b). In the  $R32-TiH_3$ , H atoms at Wyckoff positions of 1a and 1b are located at centers of regular triangles, each formed by three Ti atoms. However, in the  $R\bar{3}-TiH_3$ , the corresponding H atoms are located at 2c Wyckoff positions and protrude from the planes of regular triangles.  $TiH_{2.5}$  becomes stable when the pressure up to 18 GPa with the structure of  $Ibam$ .  $TiH_2$  maintains stability within the pressure range of 0–100 GPa, with a phase transition from  $I4/mmm$  to  $P4/nmm$  at 75 GPa of  $TiH_2$ , in line with the earlier reported transition pressure of 70 GPa by Zhuang et al. [48] and 63 GPa by Gao et al. [40]. For the stoichiometric compositions that do not stable,  $TiH_4$  still cannot be

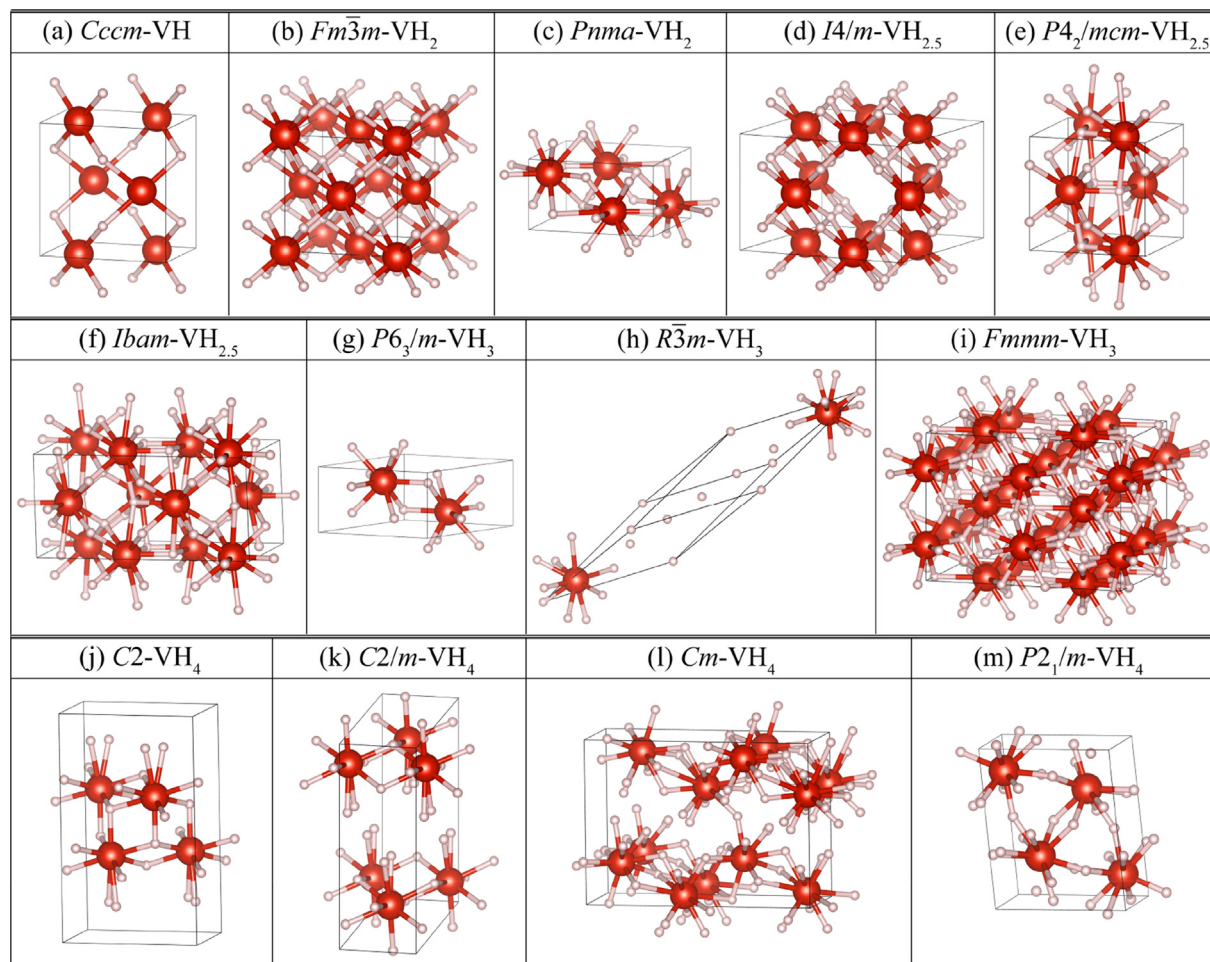


**Fig. 4** – Optimized crystal structures of V–H systems. (a) *Cccm*-VH, (b) *Fm $\bar{3}m$* -VH<sub>2</sub>, (c) *Pnma*-VH<sub>2</sub>, (d) *I4/m*-VH<sub>2.5</sub>, (e) *P4<sub>2</sub>/mcm*-VH<sub>2.5</sub>, (f) *Ibam*-VH<sub>2.5</sub>, (g) *P6<sub>3</sub>/m*-VH<sub>3</sub>, (h) *R $\bar{3}m$* -VH<sub>3</sub>, (i) *Fmmm*-VH<sub>3</sub>, (j) *C2*-VH<sub>4</sub>, (k) *C2/m*-VH<sub>4</sub>, (l) *Cm*-VH<sub>4</sub>, and (m) *P2<sub>1</sub>/m*-VH<sub>4</sub>. Red and small pink balls denote V and H atoms respectively. (For interpretation of the references to colour in this figure legend, the reader is referred to the Web version of this article.)

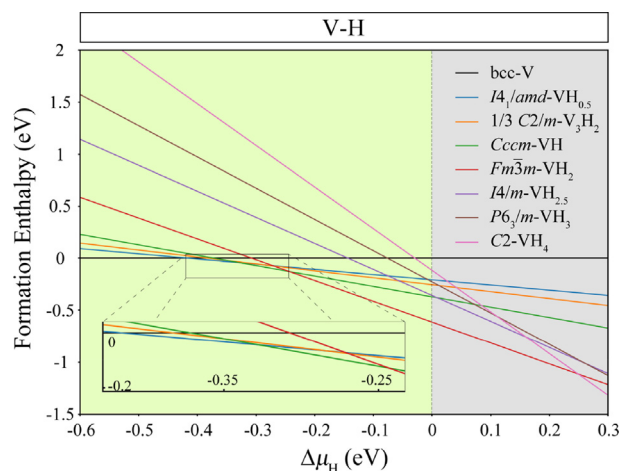


**Fig. 5** – Formation enthalpies of vanadium hydrides as a function of hydrogen chemical potential at ambient pressure. Here, chemical potential of H<sub>2</sub> is set to zero, beyond which the V–H compounds are unstable thermodynamically.

stabilized between 0 and 100 GPa and the metastable structures of *P4<sub>2</sub>/mmc*-TiH show no stability range. Remarkably, three new energetically stable structures are predicted, i.e., the *R $\bar{3}$*  phase and *P4<sub>2</sub>/mnm* phase of TiH<sub>3</sub>, and the *Ibam* phases of TiH<sub>2.5</sub>, respectively.

The calculated phonon dispersion curves of *Ibam*-TiH<sub>2.5</sub> at 20 GPa, *R $\bar{3}$* -TiH<sub>3</sub> at 50 GPa, *P4<sub>2</sub>/mnm*-TiH<sub>3</sub> at 75 GPa and *Fm $\bar{3}m$* -TiH<sub>3</sub> at 80 GPa are displayed in Fig. S7. The result shows the absence of imaginary vibrational frequencies in the Brillouin zone, indicating that these structures are dynamically stable under the corresponding pressures. The projected electronic density of states (PDOS) of those stable structures were calculated, as shown in Fig. S12. All the structures show the metallic character, with the Fermi level dominated by the Ti-3d levels. Hybridization of Ti-3d and H-1s levels is observed below the Fermi level, indicating a strong interaction between Ti and H.

#### V-H system under ambient pressure

The structures of the V-H system were predicted at ambient pressure, including VH, VH<sub>2</sub>, VH<sub>2.5</sub>, VH<sub>3</sub> and VH<sub>4</sub>. Additional

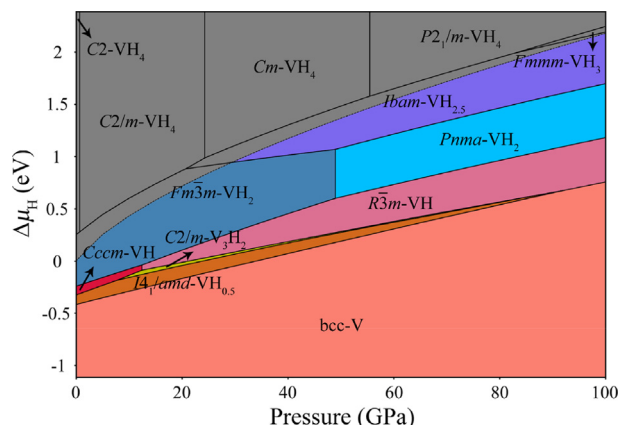


**Fig. 6 – Phase diagram of V–H system under pressure of 0–100 GPa. Structures in the gray region are unstable thermodynamically.**

calculations for structures of VH were performed because the detailed structural parameters are not available from experimental researches. Detailed structural parameters of the vanadium hydrides are listed in Table S2. The most stable structure of VH we predicted is an orthorhombic phase with *Cccm* symmetry (Fig. 4a), which is similar to the *Cccm*-NbH [21] that obtained by experiments. Occupying the 4f Wyckoff positions, V atoms form a fct sublattice ( $c/a < 1$ ) with distortion in this structure. H atoms located at the 4b Wyckoff positions, occupy half of the tetrahedral voids of the sublattice. Each conventional cell contains four formula units. For  $\text{VH}_2$ , the famous *Fm3m* fluorite structure (Fig. 4b), is found as the most stable phase under ambient pressure, which is consistent with the previous experimental result [23]. The fluorite

structure contains four formula units in each conventional cell. V and H atoms are located at the 4a and 8c Wyckoff positions respectively. V atoms form a fcc sublattice where the H atoms occupy all of the tetrahedral voids. The tetragonal structure *I4/m* (Fig. 4d), has the lowest enthalpy for  $\text{VH}_{2.5}$  at ambient pressure that can be seen as the *Fm3m*- $\text{VH}_2$  with one-fifth of V atoms lost. This structure contains eight V atoms and twenty H atoms in each conventional cell, composed of the distorted V-centered  $\text{VH}_8$  cube. One-fifth of the H atoms occupy tetrahedral voids at the 4d positions, while the others are located at the 16i positions, each surrounded by three V atoms. The hexagonal *P6\_3/m* (Fig. 4g) is the most stable phase of  $\text{VH}_3$  we found, and it has almost the same structure as *P6\_3/m*- $\text{TiH}_3$ . The most stable structure of  $\text{VH}_4$  is a layered monoclinic C2 phase (Fig. 4j), which has similar polyhedrons to the *C2/m*- $\text{TiH}_4$ . Each conventional cell contains four formula units. V atoms form two close-packed plane of hcp structure in each layer. The shortest H-H distance in the  $\text{VH}_9$  polyhedrons is 0.810 Å at ambient pressure. The pairs of H atoms which have the shortest separation are located at the surfaces of the layers and have two different orientations depending on which side of surfaces they located at.

Formation enthalpy with respect to the bcc phase of V and the  $\text{H}_2$  molecule were calculated to evaluate the stability of different stoichiometry for vanadium hydrides, as shown in Fig. 5. The experimental structures, *I4\_1/amd*- $\text{VH}_{0.5}$  [32] and *C2/m*- $\text{V}_3\text{H}_2$  [23], were also considered in this calculation as the low hydrogen content vanadium hydrides. It is indicated that V,  $\text{VH}_{0.5}$ , VH and  $\text{VH}_2$  can be stable under ambient pressure, consistent with previous experimental results, i.e., higher hydrogen content vanadium hydrides cannot be obtained at ambient pressure. Therefore, we try to find vanadium hydrides under high pressure.

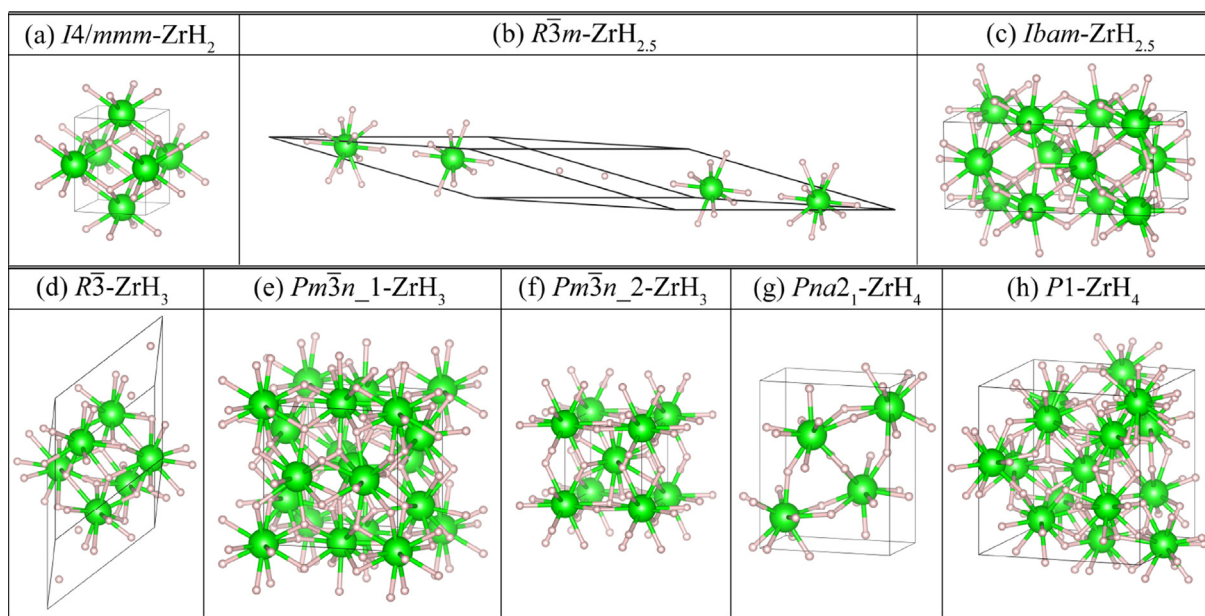


**Fig. 7 – Optimized crystal structures of Zr-H systems. (a) *I4/mmm*- $\text{ZrH}_2$ , (b) *R3m*- $\text{ZrH}_{2.5}$ , (c) *Ibam*- $\text{ZrH}_{2.5}$ , (d) *R3*- $\text{ZrH}_3$ , (e) *Pm3n\_1*- $\text{ZrH}_3$ , (f) *Pm3n\_2*- $\text{ZrH}_3$ , (g) *Pna2\_1*- $\text{ZrH}_4$ , and (h) *P1*- $\text{ZrH}_4$ . Lime and pink balls denote Zr and H atoms respectively. (For interpretation of the references to colour in this figure legend, the reader is referred to the Web version of this article.)**

## V-H system at high pressure

The structures of  $\text{VH}_x$  ( $x = 1, 2, 2.5, 3, 4$ ) were searched up to 100 GPa. The predicted structures are displayed in Fig. 4 and the calculated enthalpies curves are shown in Fig. S3.

The experimental results show that VH has a sublattice of bct composed of V atoms, while H atoms tend to occupy the octahedral voids of the sublattice at 0 K [23]. However, more detailed crystal structure information is lacking. A common inferred structure with  $I4/mmm$  symmetry [65,66] is shown in Fig. S1c. It is a metastable phase according to our calculations (see Fig. S3a). The  $Cccm$ -VH (Fig. 4a) found at ambient pressure is the most favorable under 0–13 GPa. When pressure up to 13 GPa, the trigonal  $R\bar{3}m$  phase (Fig. S1b) becomes the most stable VH, which contains one formula unit for each conventional cell with atoms of V at 1a (0, 0, 0) and H at 1b (0.5, 0.5, 0.5) positions, reported by Li and Peng [52], and Zhuang et al. [49] as a high-pressure stable phase.

The orthorhombic  $Pnma$  phase (Fig. 4c) becomes the most stable  $\text{VH}_2$  when pressure up to 49 GPa. In this structure, each conventional cell contains four formula units. V atoms located at 4c Wyckoff positions, form a hcp sublattice with distortion. Half of the H atoms are situated in the tetrahedral sites of the sublattice, while the rest of the H atoms are located at the octahedral sites.

The  $I4/m$ - $\text{VH}_{2.5}$  (Fig. 4d) is more favorable between 0 and 6 GPa. When the pressure between 6 and 15 GPa, a tetragonal  $P4_2/mcm$  phase (Fig. 4e) has the lowest enthalpies in many structures of  $\text{VH}_{2.5}$ . In this structure, each conventional cell contains four V atoms and ten H atoms. V atoms located at the 4i Wyckoff positions form a fct sublattice with distortion. H atoms are located at the 4e, 4j, 2b Wyckoff positions, respectively. In the pressure range of 15–100 GPa, an orthorhombic  $Ibam$  phase (Fig. 4f) is more stable. This phase is similar to the  $Ibam$ - $\text{TiH}_{2.5}$  in symmetry and occupied Wyckoff positions. The  $P4_2/mcm$ - $\text{VH}_{2.5}$  and the  $Ibam$ - $\text{VH}_{2.5}$  consist of  $\text{VH}_{10}$  polyhedrons, with different arrangement. The enthalpy difference between the two structures is less than 0.014 eV per  $\text{VH}_{2.5}$  when the pressure is lower than 100 GPa.

The hexagonal  $P6_3/m$  (Fig. 4g), the most stable phase of  $\text{VH}_3$  under 0–13 GPa, has a phase transition at pressure of 41 GPa. The symmetry becomes  $P6_3/mmc$  as the positions of H atoms shift with the pressure, in analogy with  $P6_3/m$ - $\text{TiH}_3$ . For the other low enthalpy structures of  $\text{VH}_3$ , the trigonal  $R\bar{3}m$  phase (Fig. 4h) with a layered structure, which contains two formula units in each conventional cell, is the most stable phase between 13 and 48 GPa. Structurally, V atoms, each surrounded by ten H atoms, form a fragment of hcp which consist of two adjacent and complete close-packed planes in a layer. One-sixth of H atoms, located at octahedrons between the two close-packed planes, occupy the 1b positions. The H atoms surrounded by three V atoms are located at the surface of the layers. The rest of the H atoms occupy the 1a positions which are between two V atoms from two different layers. Up to 48 GPa, the  $Fmmm$  phase (Fig. 4i) of  $\text{VH}_3$ , which contains sixteen formula units in each conventional cell is the most stable, reported by Zhuang et al. [49] as a stable phase under high pressure. This structure composed by  $\text{VH}_{10}$  polyhedrons with V atoms located at 8i Wyckoff positions, and  $\text{VH}_{12}$

polyhedrons with V atoms located at 8e sites. V atoms form a bct sublattice with distortion. For the hydrogen, H atoms situated in 16k and 8h positions, occupy the tetrahedral voids of the sublattice. Another one-sixth of H atoms situated in 8g positions, are located in the octahedron voids but deviating from the center. The others are situated in 16m Wyckoff positions, each surrounded by three V atoms. The  $Fm\bar{3}m$  phase, reported by Li and Peng [52], and Zhuang et al. [49] as a high-pressure stable phase, is found to be a more favorable structure of  $\text{VH}_3$  when the pressure is over 100 GPa. This structure also appeared from the prediction of  $\text{TiH}_3$ .

The mentioned  $C2$ - $\text{VH}_4$  (Fig. 4j) is more favorable in the range of 0–0.7 GPa. When the pressure is between 0.7 and 24 GPa, the most stable phase of  $\text{VH}_4$  is the monoclinic  $C2/m$  (Fig. 4k) structure, which appeared for  $\text{TiH}_4$  too. Between 24 and 55 GPa, the monoclinic  $Cm$  structure (Fig. 4l) which contains eight formula units in each conventional cell, is the most stable structure of  $\text{VH}_4$ . Up to 55 GPa, the  $P2_1/m$  structure (Fig. 4m) with the lowest enthalpy of  $\text{VH}_4$  consisted of two kinds of  $\text{VH}_{11}$  polyhedrons, has a similar structure to the orthorhombic  $Pnma$ - $\text{TiH}_4$ . The monoclinic  $Pm$  structure (Fig. S1d), composed of three kinds of  $\text{VH}_{12}$  and one kind of  $\text{VH}_{11}$ , has a tendency to become the most stable  $\text{VH}_4$  with the increasing pressure. The enthalpy difference between the  $Pm$  and  $P2_1/m$  phases is less than 0.002 eV per  $\text{VH}_4$  at 100 GPa.

The  $P$ - $\Delta\mu_{\text{H}}$  phase diagram of V-H system is illustrated in Fig. 6, with the pressure ranged from 0 to 100 GPa. The bcc phase and the hexagonal  $P6_3/m$  phase were considered for V [23] and H [64] respectively, after the comparison on the structures of V and  $\text{H}_2$  under different pressure. High-pressure phases of low hydrogen content hydrides were not considered. The chemical potential of  $\text{H}_2$  molecule at 0 GPa is set to zero and the chemical potential of  $P6_3/m$ -H is plotted as a dashed line. The gray area above zero point represents the chemical potential of H atoms is too high to reach. Different phases are separated by solid lines. The result shows that  $\text{VH}_{2.5}$  with the structure of  $Ibam$  is stable above 29 GPa. In previous research, Li and Peng [52] also found a  $\text{VH}_{2.5}$  with  $Ibam$  symmetry but the stability range is from 53 to 200 GPa. We are not sure if the two structures are the same, as the detailed Wyckoff sites were not given in literature. The phase transition of  $\text{VH}_2$  from  $Fm\bar{3}m$  to  $Pnma$  is predicted at 49 GPa, in line with the previous result [39,49,52]. VH can be stable in the whole pressure range. The  $Cccm$ -VH is stable from 0 to 13 GPa, while its  $R\bar{3}m$  phase is stable from 13 to 100 GPa. In previous work, only the  $R\bar{3}m$  structure at high pressure is predicted for VH [49,52]. Both the experimental structures of  $C2/m$ - $\text{V}_3\text{H}_2$  and  $I4_1/amd$ - $\text{VH}_{0.5}$  have their stability ranges in our calculated phase diagram (c.f. Fig. 5). The specific stability ranges do not make much sense since high-pressure phases of the low hydrogen content hydrides were not considered. Although  $\text{VH}_3$  does not have a stability range, it has a tendency to enter the stable area as the pressure increases. In a previous work, Li and Peng [52] predicted that  $\text{VH}_3$  can be stable above 127 GPa with the  $Fm\bar{3}m$  structure. Zhuang et al. [49] predicted the  $\text{VH}_3$  is stable at 50 GPa with  $Fmmm$  symmetry since they did not consider the influence of  $\text{VH}_{2.5}$ . No stable  $\text{VH}_4$  is predicted, which is in agreement with the previous result.

The calculated phonon dispersion curves for *Cccm*-VH at 0 GPa and *Ibam*-VH<sub>2.5</sub> at 30 GPa are shown in Fig. S8. The result shows that all of these structures have no imaginary frequencies, confirming their dynamical stability under the corresponding pressure. We calculated the PDOS for the *Cccm*-VH and *Ibam*-VH<sub>2.5</sub> at their corresponding pressure as shown in Fig. S13. The electronic density state at the Fermi level shows that both of the hydrides are metallic. The Fermi level is dominated by the V-3d levels. Hybridization for V-3d and H-1s levels is observed below the Fermi level, indicating covalent bonds between V and H.

### Zr-H system under ambient pressure

The structures of ZrH<sub>x</sub> ( $x = 2, 2.5, 3, 4$ ) were predicted at ambient pressure. Detailed structural parameters of Zr-H compounds are presented in Table S3. The most stable structures for ZrH<sub>2</sub>, ZrH<sub>2.5</sub> and ZrH<sub>3</sub> at ambient pressure are also found in Ti-H system. They are the tetragonal *I4/mmm* phase for ZrH<sub>2</sub> (Fig. 7a), the trigonal *R3m* structure for ZrH<sub>2.5</sub> (Fig. 7b) and the trigonal *R3* phase for ZrH<sub>3</sub> (Fig. 7d). These structures have been introduced in titanium hydrogen compounds. For ZrH<sub>4</sub>, we find a novel orthorhombic *Pna21* phase (Fig. 7g) at ambient pressure. In this structure, each Zr atom is surrounded by eleven H atoms. There are three-quarters of H atoms, each surrounded by three Zr atoms, and each of the others is located between two Zr atoms. This phase and the *Pnma*-TiH<sub>4</sub> are similar in structure, while they have different space groups due to tiny deviations in the positions of atoms.

The formation enthalpies for predicted low enthalpy phases of zirconium hydrides at ambient pressure were calculated relative to the  $\omega$  phase of zirconium solid [67] and the H<sub>2</sub> molecule, summarized in Fig. 8. A vertical dashed line passing through the zero divides the picture into two parts. The green area to the left of the dashed line represents where the chemical potential is in a reachable range, while the gray area requires unachievable conditions. The formation enthalpy of

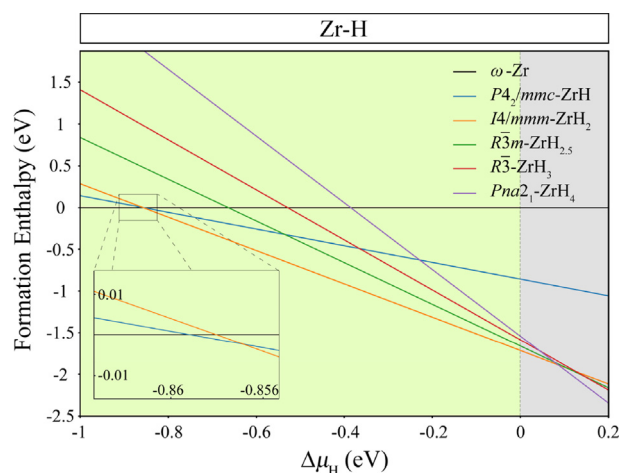


**Fig. 8** – Formation enthalpies of zirconium hydrides as a function of hydrogen chemical potential at ambient pressure. Here, chemical potential of H<sub>2</sub> is set to zero, beyond which the Zr-H compounds are unstable thermodynamically.

*P42/mmc*-ZrH [24], an experimental structure, is also illustrated for comparison. The result shows that Zr and ZrH<sub>2</sub> occupy most of the stability ranges and ZrH has a small stability range according to our calculations. The high hydrogen content zirconium hydrides of ZrH<sub>3</sub> and ZrH<sub>4</sub> are not stable at ambient pressure. It means that higher pressures are required to stabilize ZrH<sub>3</sub> or ZrH<sub>4</sub>.

### Zr-H system at high pressure

The structures of ZrH<sub>x</sub> ( $x = 2, 2.5, 3, 4$ ) were searched up to 100 GPa. The predicted structures are exhibited in Fig. 7 and the calculated enthalpies curves are shown in Fig. S4.

The mentioned *I4/mmm*-ZrH<sub>2</sub> is the most stable zirconium dihydrogen in the whole pressure range. The crystal structure is exhibited in Fig. 7a.

The *R3m* phase (Fig. 7b) is the most stable for ZrH<sub>2.5</sub> when the pressure ranges from 0 to 26 GPa. Up to 26 GPa, the most stable phase of ZrH<sub>2.5</sub> is an orthorhombic structure with *Ibam* symmetry (Fig. 7c), which has the same structure as the *Ibam*-TiH<sub>2.5</sub>.

The *R3* phase (Fig. 7d) is the most stable structure in ZrH<sub>3</sub> compounds between 0 and 19 GPa. With the increase of pressure, two cubic *Pm3n* phases are revealed. One is the most stable phase of ZrH<sub>3</sub> between 19 and 23 GPa. We refer to it as the *Pm3n\_1* (Fig. 7e). The other is more favorable when pressure is up to 23 GPa, reported by Li et al. [51] as a high-pressure stable phase. We refer to it as the *Pm3n\_2* (Fig. 7f). Both phases are composed by ZrH<sub>12</sub> polyhedrons. The structure of *Pm3n\_2*-ZrH<sub>3</sub> is simpler: each conventional cell contains two formula units and Zr atoms form a bcc sublattice where H atoms occupy half of the tetrahedral voids at the 6d positions. In the structure of *Pm3n\_1*, each conventional cell contains eight Zr atoms and twenty-four H atoms. The Zr atoms, which are located at the vertices and center of the conventional cell, occupy the 2a positions. The other Zr atoms located at the faces of the conventional cell, occupy the 6d Wyckoff positions. H atoms are located at 24k positions, each surrounded by four Zr atoms. The *Fm3m* phase of ZrH<sub>3</sub>, which is the same structure as the cubic *Fm3m*-TiH<sub>3</sub>, is also found in this work, but it is not the most stable below 100 GPa.

The *Pna21* structure (Fig. 7g) is the most favorable for ZrH<sub>4</sub> in the pressure range of 0–20 GPa. When the pressure increases to 20 GPa, a triclinic *P1* phase (Fig. 7h) whose conventional cell contains sixteen ZrH<sub>4</sub> formula units, has the lowest enthalpy in all the predicted ZrH<sub>4</sub> structures. In this structure, every Zr atom is surrounded by over twelve H atoms. The low symmetry of the new structure implies the existence of a lower enthalpy structure with a larger conventional cell.

The  $P-\Delta\mu_H$  phase diagram of Zr-H system was calculated from 0 to 100 GPa, as shown in Fig. 9. The chemical potential of H<sub>2</sub> molecule at 0 GPa is set to zero. We considered the hexagonal *P63/m* phase for H [64] to obtain the chemical potential of H atoms under high pressure, as shown as a dashed line in the plot. For Zr, the  $\omega$  phase [67], bct phase [68] and bcc phase [24] were used as references from 0–26 GPa, 26–31 GPa, and 31–100 GPa, respectively (shown in Fig. S6b). High-pressure phases of low hydrogen content hydrides were not considered. The colored area denotes a region where the chemical

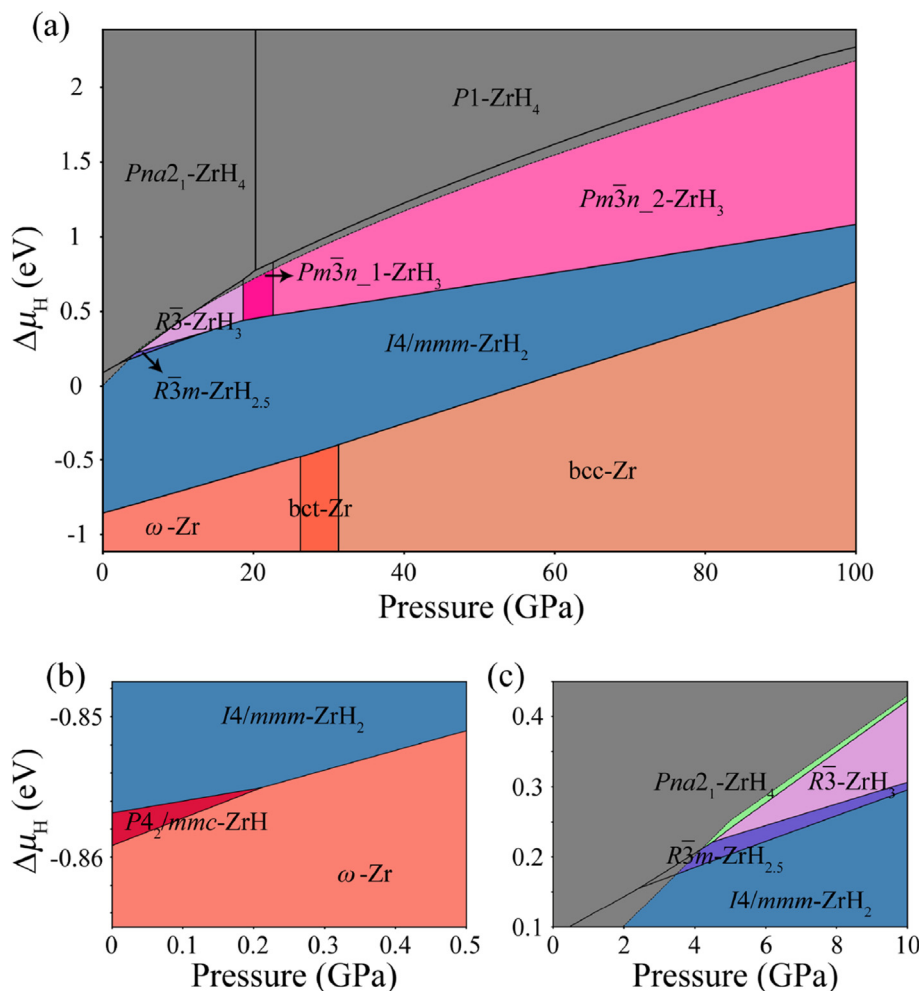


**Fig. 9** – (a) Phase diagram of Zr-H system under pressure of 0–100 GPa. Structures in the gray region are unstable thermodynamically. Partial enlargement of the phase diagram to highlight (b) the  $P4_2/mmc$ -ZrH and (c) the  $Pna2_1$ -ZrH<sub>4</sub>.

potential of H atoms is reasonable. Different phases are separated by solid lines. The result shows that, ZrH<sub>4</sub> with the  $Pna2_1$  symmetry has a stability range between 4 and 12 GPa. For ZrH<sub>3</sub>, three phases are stable when the pressure up to 5 GPa: the  $R\bar{3}$  phase between 5 and 19 GPa, the  $Pm\bar{3}n_1$  phase between 19 and 23 GPa and the  $Pm\bar{3}n_2$  phase above 23 GPa. In earlier work, Li et al. [51] reported  $Pm\bar{3}n_2$ -ZrH<sub>3</sub> with a corresponding stability range from 0 to 150 GPa, while Han et al. [53] reported a  $P6_3/mmc$ -ZrH<sub>3</sub> with a stability range from 0 to 50 GPa. According to our calculations, the  $P6_3/mmc$ -ZrH<sub>3</sub> (Fig. S1e) has higher enthalpy than  $R\bar{3}$ -ZrH<sub>3</sub> and is expected to transform easily to another  $Pnma$  phase (Fig. S1f) when pressure goes up to 16 GPa, as the two phases are similar in crystal structure. The enthalpies curves are shown in Fig. S4c. The  $R\bar{3}m$  is the only stable phase of ZrH<sub>2.5</sub> and the range is 3–14 GPa. The tetragonal  $I4/mmm$  phase of ZrH<sub>2</sub> is stable in the whole range of 0–100 GPa, which is in good agreement with the previous results [38,51]. The experimental structure,  $P4_2/mmc$ -ZrH, is only stable at pressures lower than 1 GPa. In summary, we found several novel high hydrogen content zirconium hydrides, including  $Pna2_1$ -ZrH<sub>4</sub>, two phases of ZrH<sub>3</sub>, the  $R\bar{3}$  and the  $Pm\bar{3}n_1$ , and  $R\bar{3}m$ -ZrH<sub>2.5</sub>.

We calculated the phonon dispersion curves for  $R\bar{3}m$ -ZrH<sub>2.5</sub>,  $R\bar{3}$ -ZrH<sub>3</sub>,  $Pm\bar{3}n_1$ -ZrH<sub>3</sub>,  $Pm\bar{3}n_2$ -ZrH<sub>3</sub> and  $Pna2_1$ -ZrH<sub>4</sub>, at their corresponding pressures, as shown in Fig. S9. The result reveals that all of these structures have no imaginary frequencies, confirming their dynamical stability under the corresponding pressure. The calculated PDOS for ZrH<sub>4</sub>, ZrH<sub>3</sub> and ZrH<sub>2.5</sub> are illustrated in Fig. S14.  $R\bar{3}m$ -ZrH<sub>2.5</sub>,  $R\bar{3}$ -ZrH<sub>3</sub>,  $Pm\bar{3}n_1$ -ZrH<sub>3</sub>, and  $Pm\bar{3}n_2$ -ZrH<sub>3</sub> are metallic, while the exist band gap of  $Pna2_1$ -ZrH<sub>4</sub> indicates its feature of a semiconductor at 10 GPa. A strong hybridization for Zr-4d and H-1s levels below the Fermi level indicates the covalency of Zr-H bond.

#### Nb-H system under ambient pressure

The structures of NbH<sub>x</sub> ( $x = 2, 2.5, 3, 4$ ) were predicted at ambient pressure. Detailed structural parameters of Nb-H compounds are listed in Table S4. We find that the fluorite structure with  $Fm\bar{3}m$  symmetry (Fig. 10a) has the lowest enthalpy for NbH<sub>2</sub> under ambient pressure. This structure is also predicted for VH<sub>2</sub>. For NbH<sub>2.5</sub>, the tetragonal  $I4/m$  phase (Fig. 10c) is the most stable structure, which is also

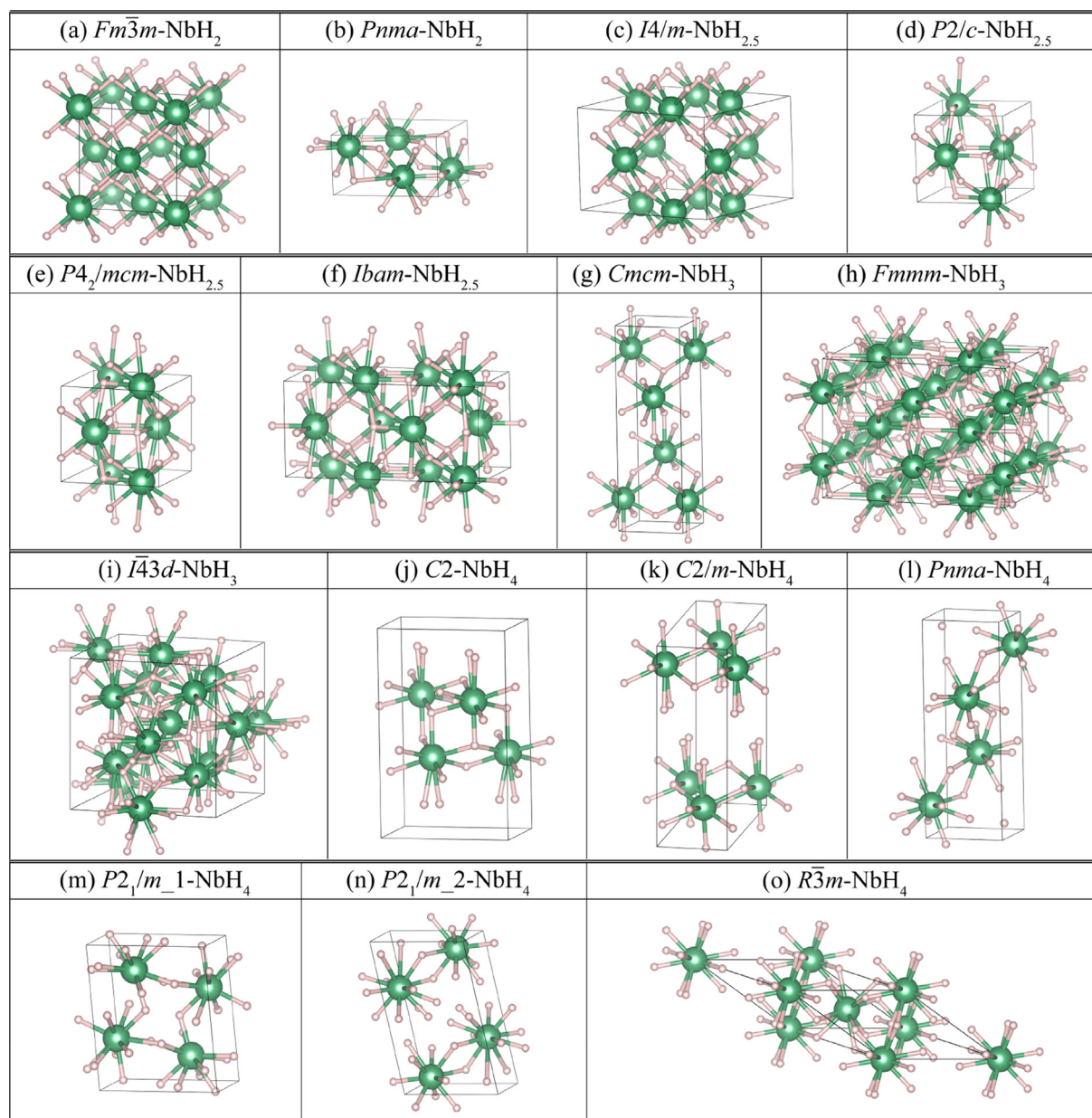


**Fig. 10** – Optimized crystal structures of Nb-H systems. (a)  $Fm\bar{3}m$ -NbH<sub>2</sub>, (b)  $Pnma$ -NbH<sub>2</sub>, (c)  $I4/m$ -NbH<sub>2.5</sub>, (d)  $P2/c$ -NbH<sub>2.5</sub>, (e)  $P4_2/mcm$ -NbH<sub>2.5</sub>, (f)  $Ibam$ -NbH<sub>2.5</sub>, (g)  $Cmcm$ -NbH<sub>3</sub>, (h)  $Fmmm$ -NbH<sub>3</sub>, (i)  $I\bar{4}3d$ -NbH<sub>3</sub>, (j)  $C2$ -NbH<sub>4</sub>, (k)  $C2/m$ -NbH<sub>4</sub>, (l)  $Pnma$ -NbH<sub>4</sub>, (m)  $P2_1/m_1$ -NbH<sub>4</sub>, (n)  $P2_1/m_2$ -NbH<sub>4</sub>, and (o)  $R\bar{3}m$ -NbH<sub>4</sub>. Green and small pink balls denote Nb and H atoms respectively. (For interpretation of the references to colour in this figure legend, the reader is referred to the Web version of this article.)

predicted for VH<sub>2.5</sub> at ambient pressure. The orthorhombic phase with  $Cmcm$  symmetry (Fig. 10g) is found as the most stable structure of NbH<sub>3</sub> which is composed of NbH<sub>9</sub> polyhedrons. In these polyhedrons, eight of H atoms form a cube surrounding the centered Nb atom, as the remaining H atom protrudes from a face of the cube and forming a pyramid with four H atoms from the face. The NbH<sub>9</sub> polyhedrons connect with each other by common edges. Each conventional cell contains four NbH<sub>3</sub> formula units. The most stable phase of NbH<sub>4</sub> at ambient pressure has the same structure as the C2-VH<sub>4</sub>, which is layered as shown in Fig. 10j.

The formation enthalpies for the most energetically favorable structures of niobium hydrides, which were calculated with respect to the bcc phase for niobium solid and the H<sub>2</sub> molecule, is plotted in Fig. 11. The experimental phase of  $Cmcm$ -NbH [21] and the theoretical predicted P2-NbH<sub>0.75</sub> [54] are also added into the calculation for comparison. The green area to the left of the dashed line denotes the available chemical potential range. The result indicates that only Nb, NbH<sub>0.75</sub>, NbH and NbH<sub>2</sub> can be stable among different stoichiometry for niobium hydrides under ambient pressure, implying that higher pressures are required to find richer hydrogen content niobium hydrides.

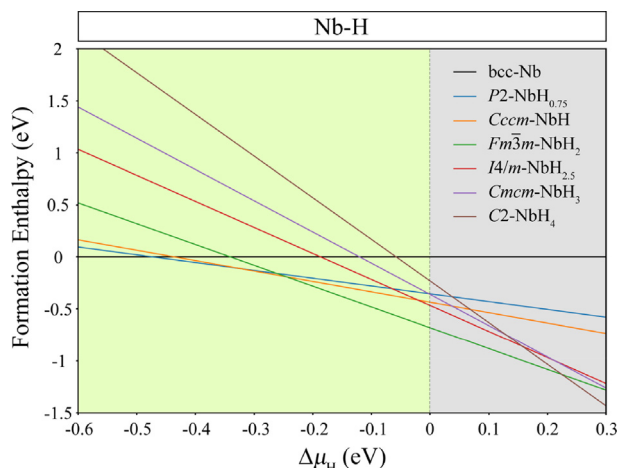


**Fig. 11** – Formation enthalpies of niobium hydrides as a function of hydrogen chemical potential at ambient pressure. Here, chemical potential of  $H_2$  is set to zero, beyond which the Nb-H compounds are unstable thermodynamically.

#### Nb-H system at high pressure

The structures of  $NbH_x$  ( $x = 2, 2.5, 3, 4$ ) were searched up to 100 GPa. The predicted structures are displayed in Fig. 10 and the calculated enthalpies curves are shown in Fig. S5.

The fluorite structure for  $NbH_2$  (Fig. 10a) is the most favorable one in the range of 0–47 GPa. A hexagonal  $P6_3/mc$  phase of  $NbH_2$  (Fig. S1h), predicted by Chen et al. [39] as a stable structure at high pressure, is the most stable  $NbH_2$  in a small range around 47 GPa. When the pressure increases to 48 GPa, the orthorhombic  $Pnma$  phase (Fig. 10b) has lower enthalpy than other structures for  $NbH_2$ . The  $Pnma-NbH_2$  and the  $Pnma-VH_2$  possess the same structure.

The  $I4/m-NbH_{2.5}$  (Fig. 10c) is the most favorable phase in the range of 0–4 GPa. Up to 4 GPa, the monoclinic  $P2/c$  phase (Fig. 10d), whose conventional cell contains four Nb atoms and ten H atoms, becomes more stable than the mentioned  $I4/m$  phase. This structure can be seen as the  $P4_2/mcm$  structure of  $VH_{2.5}$  with a slight distortion. When the pressure increases to 28 GPa, the  $P2/c-NbH_{2.5}$  becomes the tetragonal  $P4_2/mcm$  phase (Fig. 10e). When the pressure up to 41 GPa, the most stable phase of  $NbH_{2.5}$  has the same structure as the  $Ibam-TiH_{2.5}$ . The  $Ibam-NbH_{2.5}$  (Fig. 10f) was also predicted by Liu et al. [50] as a stable structure at high pressure.

The  $Cmcm$  phase (Fig. 10g) is the most stable  $NbH_3$  in the range of 0–15 GPa. When the pressure between 15 and 25 GPa, the orthorhombic phase with  $Fmmm$  symmetry (Fig. 10h), which is the same structure as the  $Fmmm-VH_3$ , becomes the most stable structure of  $NbH_3$ . Up to 25 GPa, the cubic  $I43d$  structure (Fig. 10i), whose conventional cell contains sixteen formula units, is found to be stable in  $NbH_3$ , in line with earlier results by Gao et al. [54]. Structurally, the Nb atoms are located at the 16c Wyckoff positions, each surrounded by twelve H atoms. H atoms are situated in the tetrahedral sites at the 48e Wyckoff positions. This cubic structure can also be seen as a distorted  $Pm3n$  structure (can refer to the structure of  $Pm3n_2-ZrH_3$ , shown in Fig. 7f). The cubic  $Fm3m$  phase, which is the

same structure as the cubic  $Fm3m-TiH_3$ , is also predicted for  $NbH_3$  but it is not the most stable below 100 GPa.

The C2 structure of  $NbH_4$  (Fig. 10j) we mentioned is the most stable one when the pressure is lower than 0.6 GPa. Between 0.6 and 10 GPa, the most stable structure of  $NbH_4$  (Fig. 10k) has the same symmetry and similar atomic coordinates with the monoclinic  $C2/m$  phase of  $TiH_4$ . Under the pressure between 10 and 42 GPa, the orthorhombic phase with  $Pnma$  symmetry (Fig. 10l) becomes the most stable  $NbH_4$ , in which each conventional cell contains four  $NbH_4$  formula units. Nb atoms are situated in 4c positions, each surrounded by eleven H atoms. Between 42 and 43 GPa, the monoclinic  $P2_1/m$  phase (Fig. 10m), whose conventional cell contains four  $NbH_4$  formula units, composed by Nb-centered  $NbH_{13}$  and  $NbH_{11}$  polyhedrons, is found to have the lowest enthalpy in  $NbH_4$ . We refer to it as the  $P2_1/m_1$  structure. In the pressure range of 43–62 GPa, another  $P2_1/m$  phase, which we refer to as  $P2_1/m_2$  phase (Fig. 10n), is predicted with a lower enthalpy for  $NbH_4$ . In this structure, each conventional cell contains four  $NbH_4$  formula units. The  $P2_1/m_2$  phase is composed by Nb-centered  $NbH_{10}$  and  $NbH_{13}$  polyhedrons, where the distance between the nearest H atoms is only 0.804 Å under 50 GPa. Up to 62 GPa, the trigonal  $R3m$  phase (Fig. 10o) becomes the most stable structure of  $NbH_4$  with two  $NbH_4$  formula units in each conventional cell. This structure is composed by  $NbH_{12}$  polyhedrons and  $NbH_{14}$  polyhedrons, where Nb atoms occupy the 1a and 1b Wyckoff positions of group  $R3m$ , respectively.

The  $P-\Delta\mu_H$  phase diagram of Nb-H system between 0 and 100 GPa was plotted in Fig. 12. The bcc phase [21] and the  $P6_3/m$  phase [64] were considered for the elemental Nb and H solids, respectively. The chemical potential of  $H_2$  molecule at 0 GPa is set to zero and the chemical potential of  $P6_3/m-H$  is plotted as a dashed line, which divides the phase diagram into a colored part and a gray part, representing physical and unphysical regions, respectively. High-pressure phases of low hydrogen content hydrides were not considered. The result shows that the  $NbH_3$  has one stable phase when the pressure is up to 33 GPa with the  $I43d$  symmetry, in line with the results of Gao et al. [54] For  $NbH_{2.5}$ , there are three phases having their stability ranges in the phase diagram, the  $P2/c$  phase in the range

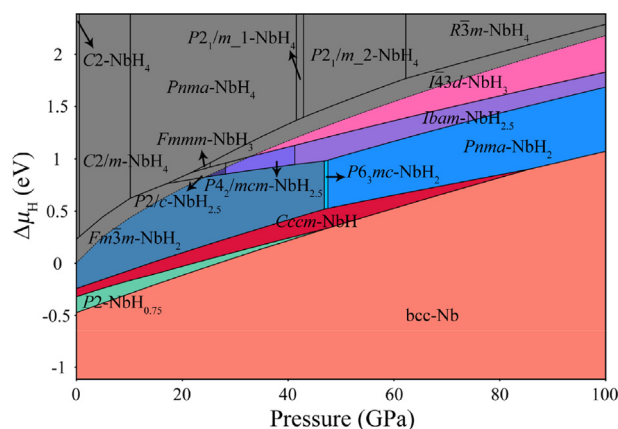


**Fig. 12** – Phase diagram of Nb-H system under pressure of 0–100 GPa. Structures in the gray region are unstable thermodynamically.

of 24–28 GPa, the  $P4_2/mcm$  phase under 28–41 GPa and the  $Ibam$  phase (also reported by Liu et al. [50]) under 41–100 GPa  $NbH_2$  is stable in the whole pressure range. The  $Fm\bar{3}m$ - $NbH_2$  is stable between 0 and 47 GPa and have a phase transition to the  $Pnma$ - $NbH_2$  at higher pressures, which is in good agreement with the result of Gao et al. [54] Chen et al. [39] predicted a phase transition of  $Fm\bar{3}m$ - $NbH_2$  to  $P6_3mc$ - $NbH_2$  at 45 GPa, and concluded that the  $P6_3mc$  structure for  $NbH_2$  can be stable up to 100 GPa. However, in our result, the  $P6_3mc$ - $NbH_2$  is stable only around 47 GPa. Both  $Cccm$ - $NbH$  and  $P2$ - $NbH_{0.75}$  have their stability ranges, in line with the results under ambient pressure.  $NbH_4$  has no stability range between 0 and 100 GPa, which is consistent with Gao et al. [54], who predicted that  $NbH_4$  is not stable until the pressure up to 287 GPa.

The phonon dispersion curves were calculated for  $P2/c$ - $NbH_{2.5}$  at 25 GPa,  $P4_2/mcm$ - $NbH_{2.5}$  at 35 GPa,  $Ibam$ - $NbH_{2.5}$  at 50 GPa and  $I\bar{4}3d$ - $NbH_3$  at 50 GPa, as displayed in Fig. S10. The absence of imaginary vibrational frequencies in the Brillouin zone indicates that these structures are dynamically stable under the corresponding pressure. The calculated PDOS of  $NbH_3$  and  $NbH_{2.5}$  indicate their metallic character, shown in Fig. S15. The result suggests that the Fermi level is dominated by the Nb-4d levels. A strong hybridization for Nb-4d, Nb-4p and H-1s levels below the Fermi level indicates the interaction between Nb and H.

## Conclusion

In summary, we report ten novel stable hydrides through first-principles calculations and structure searches: three for Ti-H system, one for V-H system, four for Zr-H system and two for Nb-H system, and several metastable phases. The  $P$ - $\Delta\mu_H$  phase diagrams were obtained for the four metal–hydrogen systems. The calculations of the phonon structures demonstrated the dynamical stability of these structures.

Meanwhile, we demonstrate that the dihydrides are the highest hydrogen content compounds obtained under ambient pressure in these four metal–hydrogen systems. Under high pressure conditions, stable structures of  $MH_{2.5}$  can be formed in all the four systems. V and H cannot form stable trihydride below 100 GPa, which implies that preparing the trihydride requires more rigorous conditions. Both Ti and Nb cannot form tetrahydride with H when the pressure is lower than 100 GPa, and the lowest pressure condition of their stable trihydride are 15 GPa and 33 GPa respectively. The trihydride are promising to obtain in experiment under today's experimental conditions. Zr is the only one that can form both tetrahydride and trihydride, and both the required pressure conditions are not exceed 5 GPa. In particular, the  $Pna2_1$ - $ZrH_4$ , a semiconductor, is found to be stable under pressure of 4 GPa, which is relatively easier to realized experimentally.

## Acknowledgments

This work is financially supported by NSFC (Grant Nos. 11574088, 51431001 and U1601212), the Foundation for Innovative Research Groups of the National Natural Science

Foundation of China (Grant No. 51621001), and Natural Science Foundation of Guangdong Province of China (Grant No. 2016A030312011).

## Appendix A. Supplementary data

Supplementary data to this article can be found online at <https://doi.org/10.1016/j.ijhydene.2019.03.210>.

## REFERENCES

- [1] Yang J, Sudik A, Wolverton C, Siegel DJ. High capacity hydrogen storage materials: attributes for automotive applications and techniques for materials discovery. *Chem Soc Rev* 2010;39:656–75. <https://doi.org/10.1039/b802882f>.
- [2] Dalebrook AF, Gan W, Grasemann M, Moret S, Laurenczy G. Hydrogen storage: beyond conventional methods. *Chem Commun* 2013;49:8735–51. <https://doi.org/10.1039/c3cc43836h>.
- [3] Drozdov AP, Erements MI, Troyan IA, Ksenofontov V, Shylin SI. Conventional superconductivity at 203 kelvin at high pressures in the sulfur hydride system. *Nature* 2015;525:73–6. <https://doi.org/10.1038/nature14964>.
- [4] Duan D, Liu Y, Tian F, Li D, Huang X, Zhao Z, et al. Pressure-induced metallization of dense  $(H_2S)_2H_2$  with high- $T_c$  superconductivity. *Sci Rep* 2014;4:6968. <https://doi.org/10.1038/srep06968>.
- [5] Liu Z, Xiong L, Li J, Liu S, Er S. Effects of alloying elements (Al, Mn, Ru) on desorption plateau pressures of vanadium hydrides: an experimental and first-principles study. *Int J Hydrogen Energy* 2018;43:21441–50. <https://doi.org/10.1016/j.ijhydene.2018.09.204>.
- [6] Kumar S, Singh PK, Kojima Y, Kain V. Cyclic hydrogen storage properties of V–Ti–Cr–Al alloy. *Int J Hydrogen Energy* 2018;43:7096–101. <https://doi.org/10.1016/j.ijhydene.2018.02.103>.
- [7] Kumar S, Jain A, Ichikawa T, Kojima Y, Dey GK. Development of vanadium based hydrogen storage material: a review. *Renew Sustain Energy Rev* 2017;72:791–800. <https://doi.org/10.1016/j.rser.2017.01.063>.
- [8] Shi F, Song X. Effect of niobium on the microstructure, hydrogen embrittlement, and hydrogen permeability of  $Nb_xHf_{(1-x)/2}Ni_{(1-x)/2}$  ternary alloys. *Int J Hydrogen Energy* 2010;35:10620–3. <https://doi.org/10.1016/j.ijhydene.2010.07.051>.
- [9] Yan E, Huang H, Min R, Xu F, Zhao P, Zou Y, et al. Design and characterizations of novel Nb–ZrCo hydrogen permeation alloys for hydrogen separation applications. *Mater Chem Phys* 2018;212:282–91. <https://doi.org/10.1016/j.matchemphys.2018.03.059>.
- [10] Towata S-i, Noritake T, Itoh A, Aoki M, Miwa K. Effect of partial niobium and iron substitution on short-term cycle durability of hydrogen storage Ti–Cr–V alloys. *Int J Hydrogen Energy* 2013;38:3024–9. <https://doi.org/10.1016/j.ijhydene.2012.12.100>.
- [11] Towata S-i, Noritake T, Itoh A, Aoki M, Miwa K. Cycle durability of Ti–Cr–V alloys partially substituted by Nb or Fe. *J Alloy Comp* 2013;580:S226–8. <https://doi.org/10.1016/j.jallcom.2013.03.163>.
- [12] Lv P, Huot J. Hydrogen storage properties of  $Ti_{0.95}FeZr_{0.05}$ ,  $TiFe_{0.95}Zr_{0.05}$  and  $TiFeZr_{0.05}$  alloys. *Int J Hydrogen Energy* 2016;41:22128–33. <https://doi.org/10.1016/j.ijhydene.2016.07.091>.

- [13] Manna J, Tougas B, Huot J. Mechanical activation of air exposed TiFe + 4 wt% Zr alloy for hydrogenation by cold rolling and ball milling. *Int J Hydrogen Energy* 2018;43:20795–800. <https://doi.org/10.1016/j.ijhydene.2018.09.096>.
- [14] Chen Z, Xiao X, Chen L, Fan X, Liu L, Li S, et al. Development of Ti–Cr–Mn–Fe based alloys with high hydrogen desorption pressures for hybrid hydrogen storage vessel application. *Int J Hydrogen Energy* 2013;38:12803–10. <https://doi.org/10.1016/j.ijhydene.2013.07.073>.
- [15] Taizhong H, Zhu W, Xuebin Y, Jinzhou C, Baojia X, Tiesheng H, et al. Hydrogen absorption–desorption behavior of zirconium-substituting Ti–Mn based hydrogen storage alloys. *Intermetallics* 2004;12:91–6. <https://doi.org/10.1016/j.intermet.2003.08.005>.
- [16] Ulmer U, Dieterich M, Pohl A, Dittmeyer R, Linder M, Fichtner M. Study of the structural, thermodynamic and cyclic effects of vanadium and titanium substitution in laves-phase AB<sub>2</sub> hydrogen storage alloys. *Int J Hydrogen Energy* 2017;42:20103–10. <https://doi.org/10.1016/j.ijhydene.2017.06.137>.
- [17] Zhang Y, Li J, Zhang T, Kou H, Xue X. Hydrogen absorption properties of a non-stoichiometric Zr-based Laves alloy against gaseous impurities. *Int J Hydrogen Energy* 2017;42:10109–16. <https://doi.org/10.1016/j.ijhydene.2017.02.040>.
- [18] Zhang Y, Li J, Zhang T, Wu T, Kou H, Xue X. Hydrogenation thermokinetics and activation behavior of non-stoichiometric Zr-based Laves alloys with enhanced hydrogen storage capacity. *J Alloy Comp* 2017;694:300–8. <https://doi.org/10.1016/j.jallcom.2016.10.021>.
- [19] Gaztañaga F, Luna CR, Orazi V, González E, Faccio R, Jasen P. Effects of native vacancies on Nb-doped MgH<sub>2</sub> using density functional theory calculations. *J Phys Chem C* 2018;122:27955–62. <https://doi.org/10.1021/acs.jpcc.8b09857>.
- [20] Floriano R, Deledda S, Hauback BC, Leiva DR, Botta WJ. Iron and niobium based additives in magnesium hydride: microstructure and hydrogen storage properties. *Int J Hydrogen Energy* 2017;42:6810–9. <https://doi.org/10.1016/j.ijhydene.2016.11.117>.
- [21] Smith JF. The H–Nb (hydrogen–niobium) and D–Nb (deuterium–niobium) systems. *Bull Alloy Phase Diagrams* 1983;4:39–46. <https://doi.org/10.1007/BF02880318>.
- [22] San-Martin A, Manchester FD. The H–Ti (hydrogen–titanium) system. *Bull Alloy Phase Diagrams* 1987;8:30–42. <https://doi.org/10.1007/BF02868888>.
- [23] Smith JF, Peterson DT. The H–V (hydrogen–vanadium) system. *Bull Alloy Phase Diagrams* 1982;3:55–60. <https://doi.org/10.1007/BF02873412>.
- [24] Zuzek E, Abriata JP, San-Martin A, Manchester FD. The H–Zr (hydrogen–zirconium) system. *Bull Alloy Phase Diagrams* 1990;11:385–95. <https://doi.org/10.1007/BF02843318>.
- [25] Song Y. New perspectives on potential hydrogen storage materials using high pressure. *Phys Chem Chem Phys* 2013;15:14524–47. <https://doi.org/10.1039/c3cp52154k>.
- [26] Machon D, Pischedda V, Le Floch S, San-Miguel A. Perspective: high pressure transformations in nanomaterials and opportunities in material design. *J Appl Phys* 2018;124:160902. <https://doi.org/10.1063/1.5045563>.
- [27] Meng D, Sakata M, Shimizu K, Iijima Y, Saitoh H, Sato T, et al. Superconductivity of the hydrogen-rich metal hydride Li<sub>3</sub>MoH<sub>11</sub> under high pressure. *Phys Rev B* 2019;99. <https://doi.org/10.1103/PhysRevB.99.024508>.
- [28] Zhang L, Wang Y, Lv J, Ma Y. Materials discovery at high pressures. *Nature Reviews Materials* 2017;2. <https://doi.org/10.1038/natrevmats.2017.5>.
- [29] Bhosle V, Baburaj EG, Miranova M, Salama K. Dehydrogenation of TiH<sub>2</sub>. *Mater Sci Eng* 2003;356:190–9. [https://doi.org/10.1016/S0921-5093\(03\)00117-5](https://doi.org/10.1016/S0921-5093(03)00117-5).
- [30] Xu Q, Van der Ven A. First-principles investigation of metal-hydride phase stability: the Ti–H system. *Phys Rev B* 2007;76. <https://doi.org/10.1103/PhysRevB.76.064207>.
- [31] Ukita S, Ohtani H, Hasebe M. Thermodynamic analysis of the V–H binary phase diagram. *Mater Trans* 2008;49:2528–33. <https://doi.org/10.2320/matertrans.MB200810>.
- [32] Noda Y, Kajitani T, Hirabayashi M, Sato S. X-ray structure determination of divanadium hydride, β<sub>1</sub>-V<sub>2</sub>H, and divanadium deuteride, β-V<sub>2</sub>D. *Acta Crystallogr C* 1985;41:1566–71. <https://doi.org/10.1107/S0108270185008587>.
- [33] Orimo S-i, Kimmerle F, Majer G. Hydrogen in nanostructured vanadium-hydrogen systems. *Phys Rev B* 2001;63. <https://doi.org/10.1103/PhysRevB.63.094307>.
- [34] Terrani KA, Balooch M, Wongsawaeng D, Jaiyen S, Olander DR. The kinetics of hydrogen desorption from and adsorption on zirconium hydride. *J Nucl Mater* 2010;397:61–8. <https://doi.org/10.1016/j.jnucmat.2009.12.008>.
- [35] Zhang P, Wang B-T, He C-H, Zhang P. First-principles study of ground state properties of ZrH<sub>2</sub>. *Comput Mater Sci* 2011;50:3297–302. <https://doi.org/10.1016/j.commatsci.2011.06.016>.
- [36] Quijano R, de Coss R, Singh DJ. Electronic structure and energetics of the tetragonal distortion for TiH<sub>2</sub>, ZrH<sub>2</sub>, and HfH<sub>2</sub>: a first-principles study. *Phys Rev B* 2009;80. <https://doi.org/10.1103/PhysRevB.80.184103>.
- [37] Kanagaprabha S, Asvinimeenaatci AT, Sudhapriyanga G, JemmyCinthia A, Rajeswarapalanichamy R, Iyakutti K. First principles study of stability and electronic structure of TMH and TMH<sub>2</sub> (TM = Y, Zr, Nb). *Acta Phys Pol* 2013;123:126. <https://doi.org/10.12693/APhysPolA.123.126>.
- [38] Huang X, Duan D, Li F, Huang Y, Wang L, Liu Y, et al. Structural stability and compressive behavior of ZrH<sub>2</sub> under hydrostatic pressure and nonhydrostatic pressure. *RSC Adv* 2014;4:46780–6. <https://doi.org/10.1039/c4ra06713d>.
- [39] Chen C, Tian F, Duan D, Bao K, Jin X, Liu B, et al. Pressure induced phase transition in MH<sub>2</sub> (M = V, Nb). *J Chem Phys* 2014;140:114703. <https://doi.org/10.1063/1.4866179>.
- [40] Gao G, Bergara A, Liu G, Ma Y. Pressure induced phase transitions in TiH<sub>2</sub>. *J Appl Phys* 2013;113:103512. <https://doi.org/10.1063/1.4795164>.
- [41] Zhu L, Wang Z, Wang Y, Zou G, Mao H-k, Ma Y. Spiral chain O<sub>4</sub> form of dense oxygen. *Proc Natl Acad Sci U S A* 2012;109:751–3. <https://doi.org/10.1073/pnas.1119375109>.
- [42] Liu H, Wang H, Ma Y. Quasi-molecular and atomic phases of dense solid hydrogen. *J Phys Chem C* 2012;116:9221–6. <https://doi.org/10.1021/jp301596v>.
- [43] Zhang X, Qin J, Liu H, Zhang S, Ma M, Luo W, et al. Pressure-induced zigzag phosphorus chain and superconductivity in boron monophosphide. *Sci Rep* 2015;5:8761. <https://doi.org/10.1038/srep08761>.
- [44] Li X, Hermann A, Peng F, Lv J, Wang Y, Wang H, et al. Stable lithium argon compounds under high pressure. *Sci Rep* 2015;5:16675. <https://doi.org/10.1038/srep16675>.
- [45] Liu Z, Botana J, Hermann A, Valdez S, Zurek E, Yan D, et al. Reactivity of He with ionic compounds under high pressure. *Nat Commun* 2018;9:951. <https://doi.org/10.1038/s41467-018-03284-y>.
- [46] Ma Y, Duan D, Shao Z, Li D, Wang L, Yu H, et al. Prediction of superconducting ternary hydride MgGeH<sub>6</sub>: from divergent high-pressure formation routes. *Phys Chem Chem Phys* 2017;19:27406–12. <https://doi.org/10.1039/c7cp05267g>.
- [47] Zhang S, Zhu L, Liu H, Yang G. Structure and electronic properties of Fe<sub>2</sub>SH<sub>3</sub> compound under high pressure. *Inorg Chem* 2016;55:11434–9. <https://doi.org/10.1021/acs.inorgchem.6b01949>.
- [48] Zhuang Q, Jin X, Cui T, Zhang D, Li Y, Li X, et al. Effect of electrons scattered by optical phonons on superconductivity

- in  $MH_3$  ( $M = S, Ti, V, Se$ ). *Phys Rev B* 2018;98. <https://doi.org/10.1103/PhysRevB.98.024514>.
- [49] Zhuang Q, Jin X, Lv Q, Li Y, Shao Z, Liu Z, et al. Investigation of superconductivity in compressed vanadium hydrides. *Phys Chem Chem Phys* 2017;19:26280–4. <https://doi.org/10.1039/c7cp03435k>.
- [50] Liu G, Besedin S, Irodova A, Liu H, Gao G, Eremets M, et al. Nb-H system at high pressures and temperatures. *Phys Rev B* 2017;95. <https://doi.org/10.1103/PhysRevB.95.104110>.
- [51] Li X-F, Hu Z-Y, Huang B. Phase diagram and superconductivity of compressed zirconium hydrides. *Phys Chem Chem Phys* 2017;19:3538–43. <https://doi.org/10.1039/c6cp08036g>.
- [52] Li X, Peng F. Superconductivity of pressure-stabilized vanadium hydrides. *Inorg Chem* 2017;56:13759–65. <https://doi.org/10.1021/acs.inorgchem.7b01686>.
- [53] Han Z-z, Lu Y, Wang W, Hou Z-l, Shao X-h. The novel structure and superconductivity of zirconium hydride. *Comput Mater Sci* 2017;134:38–41. <https://doi.org/10.1016/j.commatsci.2017.03.021>.
- [54] Gao G, Hoffmann R, Ashcroft NW, Liu H, Bergara A, Ma Y. Theoretical study of the ground-state structures and properties of niobium hydrides under pressure. *Phys Rev B* 2013;88. <https://doi.org/10.1103/PhysRevB.88.184104>.
- [55] Wang Y, Lv J, Zhu L, Ma Y. CALYPSO: a method for crystal structure prediction. *Comput Phys Commun* 2012;183:2063–70. <https://doi.org/10.1016/j.cpc.2012.05.008>.
- [56] Wang Y, Lv J, Zhu L, Ma Y. Crystal structure prediction via particle-swarm optimization. *Phys Rev B* 2010;82. <https://doi.org/10.1103/PhysRevB.82.094116>.
- [57] Momma K, Izumi F. VESTA 3 for three-dimensional visualization of crystal, volumetric and morphology data. *J Appl Crystallogr* 2011;44:1272–6. <https://doi.org/10.1107/S0021889811038970>.
- [58] Perdew JP, Burke K, Ernzerhof M. Generalized gradient approximation made simple. *Phys Rev Lett* 1996;77:3865–8. <https://doi.org/10.1103/PhysRevLett.77.3865>.
- [59] Kresse G, Furthmüller J. Efficient iterative schemes for *ab initio* total-energy calculations using a plane-wave basis set. *Phys Rev B* 1996;54:11169–86. <https://doi.org/10.1103/PhysRevB.54.11169>.
- [60] Blöchl PE. Projector augmented-wave method. *Phys Rev B* 1994;50:17953–79. <https://doi.org/10.1103/PhysRevB.50.17953>.
- [61] Togo A, Tanaka I. First principles phonon calculations in materials science. *Scripta Mater* 2015;108:1–5. <https://doi.org/10.1016/j.scriptamat.2015.07.021>.
- [62] Kutepov AL, Kutepova SG. Crystal structures of Ti under high pressure: Theory. *Phys Rev B* 2003;67. <https://doi.org/10.1103/PhysRevB.67.132102>.
- [63] Wang X-Q, Wang J-T. Structural stability and hydrogen diffusion in alloys. *Solid State Commun* 2010;150:1715–8. <https://doi.org/10.1016/j.ssc.2010.06.004>.
- [64] Pickard CJ, Needs RJ. Structure of phase III of solid hydrogen. *Nat Phys* 2007;3:473–6. <https://doi.org/10.1038/nphys625>.
- [65] Paniago R, Metzger TH, Trenkler J, Hempelmann R, Reichert H, Schmid S, et al. Near-surface tricritical behavior of  $V_2H(010)$  at the  $\beta_1$ - $\beta_2$  phase transition. *Phys Rev B* 1997;56:16–9. <https://doi.org/10.1103/PhysRevB.56.16>.
- [66] Andersson PH, Fast L, Nordström L, Johansson B, Eriksson O. Theoretical study of structural and electronic properties of  $VH_x$ . *Phys Rev B* 1998;58:5230–5. <https://doi.org/10.1103/PhysRevB.58.5230>.
- [67] Zhao Y, Zhang J, Pantea C, Qian J, Daemen LL, Rigg PA, et al. Thermal equations of state of the  $\alpha$ ,  $\beta$ , and  $\omega$  phases of zirconium. *Phys Rev B* 2005;71. <https://doi.org/10.1103/PhysRevB.71.184119>.
- [68] Schönecker S, Li X, Koepernik K, Johansson B, Vitos L, Richter M. Metastable cubic and tetragonal phases of transition metals predicted by density-functional theory. *RSC Adv* 2015;5:69680–9. <https://doi.org/10.1039/c5ra14875h>.